Applied Catalysis B: Environmental 342 (2024) 123441

Contents lists available at ScienceDirect

Applied Catalysis B: Environmental

journal homepage: www.elsevier.com/locate/apcatb

A facile $MnSO_4$ surface coated $NiMnFeO_x$ catalyst with enhanced SO_2 resistance for SCR reaction: A dual-protection mechanism

Shuhao Li [a,b,c], Feng Wang [b], Derrick Ng [c], Qiqi Shi [a], Thomas J. Raeber [c], Simon James [d], Boxiong Shen [a,*], Zongli Xie [c,*]

[a] School of Energy and Environmental Engineering, Tianjin Key Laboratory of Energy Utilization and Pollutant Control, Hebei University of Technology, Tianjin 300401, China

[b] Department of Chemistry and Biotechnology, School of Science, Computing and Engineering Technologies, Swinburne University of Technology, Melbourne, VIC 3122, Australia

[c] CSIRO Manufacturing, Private Bag 10, Clayton South, VIC 3169, Australia

[d] Medium Energy X-ray spectroscopy (MEX) beamline, Australian Synchrotron, Clayton, VIC 3168, Australia

ARTICLE INFO

Keywords:
NO reduction
SO_2 resistance
Dual-protection mechanism

ABSTRACT

The SO_2 resistance under low-temperature conditions remains a pivotal challenge in the industrial application of NH_3-SCR catalysts. This work develops a facile and effective strategy of constructing a surface $MnSO_4$ coating layer on catalysts in combination with Ni doping, which significantly boosts the SO_2 resistance and stability of the conventional $MnFeO_x$ catalyst. Advanced characterizations including Synchrotron XAS analysis coupled with density functional theory (DFT) calculations, were utilized to further elucidate the underlying mechanism. The findings corroborate that the remarkable SO_2 resistance of the $MnSO_4$ surface-coated $NiMnFeO_x$ catalyst originates from a dual-protection mechanism. The doping of Ni effectively restricts the diffusion of SO_2 within the catalyst, thereby confining sulfation to the surface of the catalyst. Subsequently, the $MnSO_4$ coating layer provides further protection to the surface of the catalyst, inhibiting SO_2 adsorption and safeguarding the active metal from poisoning. Importantly, this facile strategy can be implemented without any alterations to the catalyst preparation process, making it applicable to existing commercial catalysts, thus having outstanding industrial application potential.

1. Introduction

Nitrogen oxides (NO_x) pose a direct threat to human health and indirectly contribute to environmental concerns such as acid rain, photochemical fog, and modifications to global tropospheric chemistry [1–3]. Ammonia (NH_3) selective catalytic reduction (SCR) has been well established as an efficacious post-combustion technology for the abatement of nitrogen oxides (NO_x) and there is a strong need to develop low-temperature SCR catalysts [4,5]. Mn-based catalysts have demonstrated extraordinary low-temperature performance and achieved a remarkable NO conversion of nearly 100 % at below 200 °C [6,7]. However, the manganese in the catalyst is prone to interacting with other impurities in the flue gas, leading to easy deactivation of the Mn catalytic sites. In practical applications, the reducing gas SO_2 existing in the flue gas has been identified as a primary culprit in causing the deactivation of Mn-based catalysts, thereby limiting their widespread utilization [8]. Consequently, the study of SO_2 resistance in Mn-based catalysts has remained a focal point in the realm of SCR [9,10].

Numerous strategies encompassing metal doping, support optimization, and the rational design of catalyst structure have been developed to enhance the SO_2 resistance of the catalysts. Metal doping is a prevalent solution to counteract catalyst poisoning. In this regard, cerium dioxide has been extensively investigated as an anti-sulphur additive of significant interest. The sensitive reaction of Ce with SO_2 will result in a priority absorption of SO_2 onto Ce atoms to form sulphate within flue gas. This process serves a protective role for the Brønsted and Lewis acid sites within Mn-based catalysts, mitigating the risk of catalyst poisoning [11–13]. The resistance to sulphur in catalysts can also be enhanced through the doping of other metals such as Co [14] and Fe [15]. Selecting an appropriate support is another commonly employed method for enhancing the SO_2 resistance of catalysts. The modification of supports with elements such as Zr, Fe, and W has been shown to

* Corresponding authors.
E-mail addresses: shenbx@hebut.edu.cn (B. Shen), zongli.xie@csiro.au (Z. Xie).

https://doi.org/10.1016/j.apcatb.2023.123441
Received 27 August 2023; Received in revised form 18 October 2023; Accepted 26 October 2023
Available online 28 October 2023
0926-3373/© 2023 The Authors. Published by Elsevier B.V. This is an open access article under the CC BY-NC-ND license (http://creativecommons.org/licenses/by-nc-nd/4.0/).

enhance the SO_2 resistance and activity recovery of MnO_x/Ce-Zr, MnO_x/Ce-Ti, MnO_x/Fe-Ti, and MnO_x/Ti-W catalysts [16–19]. Additionally, a significant enhancement in the SO_2 resistance performance of the catalyst can be achieved by adjusting the catalyst morphology/pore structures or constructing specialized structures. Indeed, the forefront of current research interest is the design and synthesis of catalysts featuring complex and special structures. Sophisticated structures including core-shell structure catalysts [20,21], spinel structure catalysts [22,23], nanowires, nanocages, hollow microsphere catalysts [24, 25], two-dimension structure catalysts [26] have been extensively investigated to promote the SO_2 resistance of the SCR catalysts. Selective permeation of reactants via complex pore structures in these catalysts enables the obstruction of SO_2 ingress into the catalyst, thereby preventing the active centers from deactivation.

However, each of these strategies has its own shortcomings. Metal doping has not conclusively addressed the poisoning effects of SO_2. The enhancement of SO_2 resistance is achieved by the sacrificial reaction of dopant elements with SO_2. Consequently, the catalysts may lose their optimal SO_2 resistance when these dopant elements are fully sulfonated. Support modification strategies for improving SO_2 resistance are normally realized by enhancing the dispersion and chemical state of the active metals, lacking targeted protection against SO_2. For catalysts that bolster SO_2 resistance through meticulous structural design, despite their promising prospects, their high costs pose a significant obstacle to large-scale application. Moreover, under complex operating conditions like high dust levels, their intricate pore structures are susceptible to collapse and blockage, leading inevitably to catalyst deactivation.

To address these challenges, we aimed to develop a facile, cost-effective, and robust strategy to enhance the SO_2 resistance of catalysts. In this study we successfully developed a novel approach which significantly bolsters the SO_2 resistance of the $MnFeO_x$ catalysts prepared via an ultrasound-assisted co-precipitation method. The key steps involved in this approach were twofold. Firstly, the diffusion of SO_2 within the catalyst was inhibited by Ni doping. Then, a $MnSO_4$ surface coating layer was constructed to safeguard the catalyst surface from sulfation, thereby achieving a consistent and substantial improvement in the overall SO_2 resistance of the catalysts. The SO_2 resistance mechanism of the modified catalyst was validated through rigorous density functional theory (DFT) computations and a series advanced characterization techniques including in-situ diffuse reflectance infrared Fourier transform spectroscopy (DRIFTS), X-ray photoelectron spectroscopy (XPS) and also Synchrotron sourced X-ray absorption spectroscopy (XAS).

2. Experimental

2.1. Catalyst preparation

$MnFeO_x$ (MF) and various metal doped (Ni, W, Co, Nb, Ce, Zr) catalysts were synthesized by a sonication-assisted coprecipitation method. This method has been demonstrated to significantly improve the properties and elevate the low-temperature activity of the catalysts, as documented in our prior research [27]. Taking $NiMnFeO_x$ (NMF) catalyst as an example, briefly, precursors of the catalysts ($Fe(NO_3)_3{\cdot}9\ H_2O$, $Mn(NO_3)_2{\cdot}4\ H_2O$, and $Ni(NO_3)_2{\cdot}6\ H_2O$ for NMF) were first dissolved in water under stirring, and then pumped into a high-powered (500 W, 20 kHz) ultrasound reactor together with a mixture of ammonia and ammonium bicarbonate via separate conduits. The two solutions react within the stainless steel-encased continuous flow cell of the reactor, leading to the formation of a slurry. The slurry was then collected and allowed to age for 12 h before undergoing three water washes and one acetone wash in a centrifuge machine. The washed precipitate was then dried at room temperature for over 24 h, after which it was calcined at 500 °C for 3 h in a furnace in air. The molar ratio of Mn, Fe, and Ni for MF and NMF was set to 1:1:0 and 1:1:0.5, respectively. The $MnFeO_x$ catalysts doped with other elements (W, Co, Nb, Ce, Zr) were synthesized using the same method, with only the precursors changed. The ratio of the doping elements to Fe and Mn was maintained the same as in NMF.

The $MnSO_4$-coated catalysts were synthesized via the wet impregnation method. The catalyst powder ($WMnFeO_x$ or $NiMnFeO_x$) was introduced into the aqueous solutions of $MnSO_4$. The resulting mixture was then agitated at 70 °C until complete dryness. The resulting catalysts were denoted as WMFS and NMFS, respectively.

2.2. Activity test

The NH_3-SCR performance of the synthesized catalysts was systematically evaluated in a stainless-steel tubular downflow reactor, as shown in Fig. S1. The reaction gas was composed of NO (500 ppm), NH_3 (500 ppm), and O_2 (3 vol%), balanced by N_2, and the GHSV was kept at 60,000 h^{-1}. The reaction gas was further tailored to include 5 wt% H_2O and 200 ppm SO_2 when specified. The concentration of the effluent gas was continually assessed with the aid of a flue gas analyser (Kane 905, Kane International, UK) and N_2O analyser (Model 46i-HL, Thermo Fisher Scientific, US). Prior to every batch of experiments, the calibration of the equipment was maintained. For the activity tests, each catalytic experiment was conducted in triplicate to ensure reliability, and the calculated corresponding error limits were depicted in the figures (Fig. 1a). For the stability tests, the concentration of each component inside the reactor was continuously monitored and logged every 30 s. The stability test for each catalyst was double-checked to ensure the reliability of the stability results obtained. Any significant discrepancies between two test results were re-evaluated to determine the potential reasons for the difference. Control experiments were also conducted without the catalyst to evaluate any potential non-catalytic reactions or interferences that could impact our results. The NO conversion and N_2 selectivity were determined based on the following respective equations:

$$\text{NO conversion} = \frac{NO_{in} - NO_{out}}{NO_{in}} * 100\% \quad (1)$$

$$N_2\ \text{selectivity} = 100\% - \frac{2 * N_2O_{out} + NO_{2out}}{NO_{in} - NO_{out}} \quad (2)$$

NO_{in}, NO_{out}, NO_{2out} and N_2O_{out} represent the inlet concentration of NO, outlet concentration of NO, NO_2, and N_2O, respectively.

2.3. Catalyst characterization

The Brunauer–Emmett–Teller (BET) surface area and pore size of the catalysts were analysed using nitrogen physisorption measurement on a high vacuum physisorption/chemisorption analyser (MP, Autosorb iQ, USA). Crystalline structure analysis was conducted via X-ray Diffraction (XRD) experiments using a Bruker D8 Advance A25 X-ray Diffractometer with CuKα radiation (40 kV, 40 mA). Elemental composition was assessed with an Inductively Coupled Plasma Optical Emission Spectroscopy (ICP-OES) test (Varian, 730-ES ICP-OES). Scanning Electron Microscope (SEM) images were captured using a MERLIN ZEISS Gemini 2 microscope, operated at a voltage of 3.5 kV and a working distance of 6 mm. The elemental mappings and energy-dispersive X-ray spectroscopy (EDS) data were obtained utilizing the AZtec analysis software. The thermogravimetric analysis (TGA) was conducted using a Mettler Toledo TGA-2 system. Samples were placed in alumina holders and heated from 25 °C to 900 °C at a heating rate of 10 K/min. The experiment was conducted under a nitrogen purge gas with a flow rate of 50 mL/min. H_2-Temperature programmed reduction (H_2-TPR) analysis was conducted utilizing a PSs Micromeritics Chemisorb 2750 TPx system. The temperature was ramped at a rate of 20 °C/min up to 700 °C, and the hydrogen consumption due to adsorption or reaction was subsequently monitored and quantified using a thermal conductivity detector (TCD).

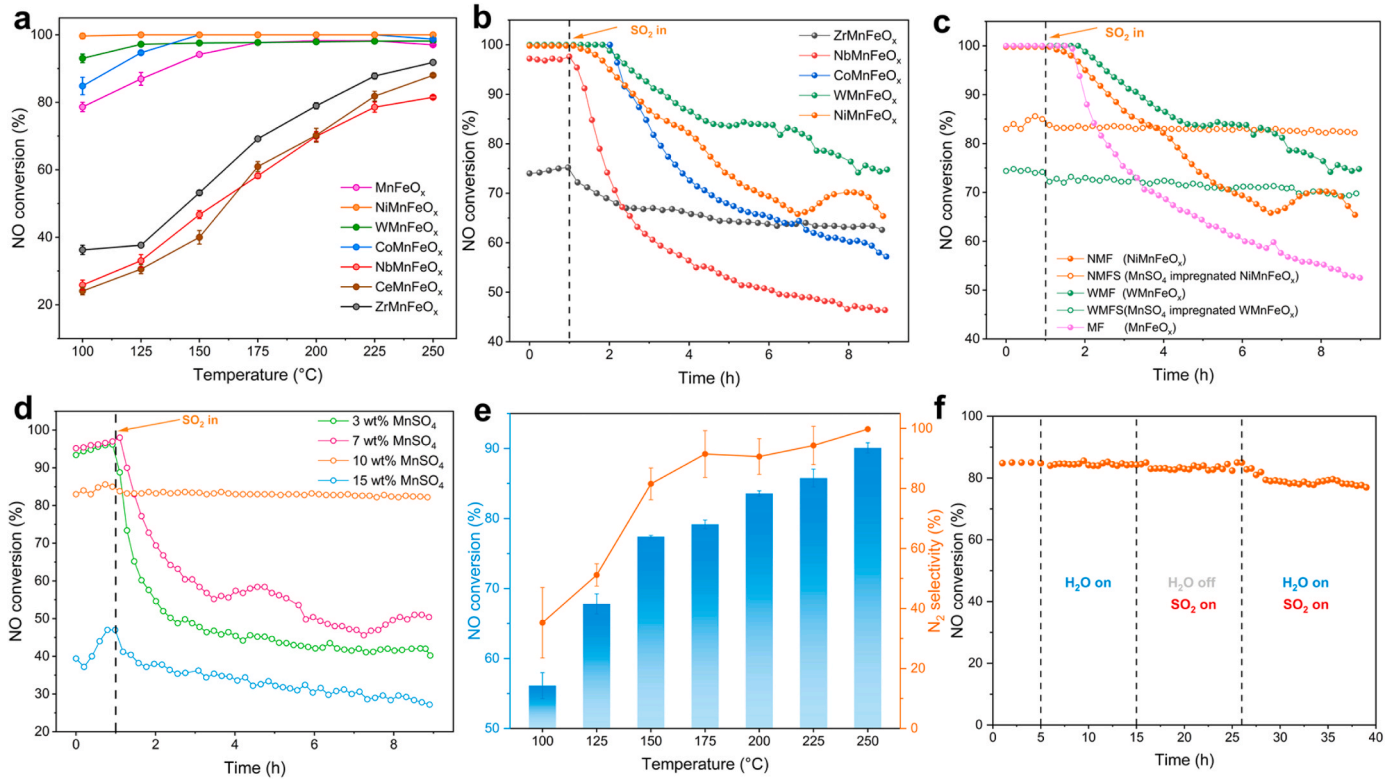

Fig. 1. Catalytic activity and stability. (a) NO conversion of $MnFeO_x$ catalysts doped with different elements. SO_2 resistance of (b) catalysts with different doping elements, (c) $MnSO_4$-coated $NiMnFeO_x$ (NMFS) and $WMnFeO_x$ (WMFS) catalysts, and (d) NMFS catalysts with different $MnSO_4$ coating amounts. (e) NO conversion and N_2 selectivity and (f) long-term H_2O/SO_2 stability of the NMFS catalysts. Reaction conditions: 500 ppm NO and NH_3, 3 vol% O_2, 200 ppm SO_2 (when used), 5 vol % H_2O (when used), GHSV = 60,000 h^{-1}. The reaction temperature of all the stability tests was set to 225 °C.

X-ray photoelectron spectroscopy (XPS) analysis was performed on a Kratos AXIS Ultra spectrometer (Kratos Analytical Inc., UK) with a monochromated Al Kα source operated at a power of 180 W (15 kV × 12 mA). The hemispherical analyser was operated in the fixed analyser transmission mode and the main vacuum chamber pressure was typically between 10^{-9} and 10^{-8} mbar during analysis. Survey spectra were acquired at a pass energy of 160 eV and step of 0.5 eV. To obtain information on the chemical states, higher resolution narrow scans were performed at 20 eV with a step of 0.1 eV. All measurements were taken with an emission angle of 0 ° (surface normal). The data processing was performed using CasaXPS version 2.3.23 (Casa Software Ltd., Teignmouth, UK). The peak binding energies were referenced to the C 1 s peak at 284.8 eV.

X-ray absorption spectroscopy (XAS) experiments were performed on the Medium Energy X-ray Absorption Spectroscopy (MEX-1) beamline stationed at the Australian Synchrotron (AS). The X-ray absorption near edge structure (XANES) and extended X-ray absorption fine structure (EXAFS) data for Mn and Fe K-edge were meticulously acquired in transmission mode under ambient conditions. The subsequent interpretation of XAS data was facilitated using the ATHENA software suite [28]. To ensure appropriate normalization and alignment, XANES spectra were calibrated against the edge jump utilizing the spectra of standard foils. The wavelet transform (WT) study of EXAFS was accomplished using the HAMA Fortran package [29].

In situ diffuse reflectance infrared spectroscopy (in situ DRIFTS) studies were conducted using a DRIFTS cell from Harrick Scientific, and the functional groups were detected by an FT-IR spectrometer (TENSOR II, Bruker, Germany). Prior to the test, the catalyst was purged in a N_2 flow at 400 °C for one hour to remove impurities. The catalyst was then cooled to room temperature and the infrared spectrum was recorded at the respective temperature as the background spectrum. In the formal test, the background spectrum at the corresponding temperature was subtracted. Following this, a continuous feed of SO_2 (200 ppm) and O_2 (3 %) was added to the flue gas (balance with N_2). Spectra were continually recorded every minute for a total duration of 60 min.

2.4. DFT calculation

The Vienna ab initio simulation package (VASP) was employed for executing spin-polarized DFT computations. Perdew-Burke-Ernzerhof (PBE) function in conjunction with the generalized gradient approximation (GGA) was employed to deal with the exchange-correlation interaction. The projector augmented wave (PAW) potentials were applied to characterize the electron-ion interactions, setting the cut-off energy for plane-wave basis sets to 450 eV across all calculations. The localized behavior of the Mn 3d orbitals is depicted using the DFT+U approach with a U value set at 3.9 eV [30]. The (2 1 1) surface of the $NiMnFeO_x$ (NMF) catalyst, which is most likely to be exposed, was chosen to construct the periodic slab for calculations. A 15 Å vacuum slab was applied along the z-direction to the surface slabs to remove the effects of interaction between neighboring supercells. A gamma-pack k-mesh of 4 × 3 × 1 and 3 × 2 × 1 was implemented to sample the Brillouin zones for projected density of states (PDOS) and other calculations, respectively. The adsorption energy (E_{ads}) of SO_2 on the catalyst surface was calculated as:

$$E_{ads} = E_{total} - E_{slab} - E_{adsorbate} \quad (3)$$

Where E_{total}, E_{slab}, and $E_{adsorbate}$ are the total energy of the SO_2 adsorbed system, catalyst slabs, and SO_2 molecule, respectively.

The valence charge density difference (VCDD) maps of NMFS and SO_2 adsorbed catalysts are depicted based on the charge density difference ($\Delta\rho$) defined in Eqs. (4) and (5), respectively.

$$\Delta\rho = \rho_{cat} - \rho_{slab} - \rho_{MnSO_4} \quad (4)$$

$$\Delta\rho = \rho_{cat} - \rho_{slab} - \rho_{SO_2} \quad (5)$$

The ρ_{cat}, ρ_{slab}, ρ_{MnSO_4}, and ρ_{SO_2} represent the charge density of the whole catalyst, clean catalyst slabs, $MnSO_4$ molecule and SO_2 molecule, respectively.

The D-band centre (εd) of the catalysts was determined by the Eq. (6) using the PDOS data.

$$\varepsilon d = \frac{\int_{-\infty}^{\infty} \rho E dE}{\int_{-\infty}^{\infty} \rho dE} \quad (6)$$

3. Result and discussions

3.1. Activity and stability performance

Effect of metal doping on NO conversion and SO_2 resistance of $MnFeO_x$ (MF) catalyst was firstly evaluated and results are shown in Fig. 1a-b, respectively. As shown in Fig. 1a, catalysts doped with Ni, W, and Co exhibit enhanced low-temperature activity compared with the control MnFeOx catalyst, achieving high NO conversions of over 90 % at a low temperature of 125 °C. In contrast, the incorporation of Nb, Ce, and Zr resulted in a noticeably decreased catalytic activity across all tested temperature range. Subsequently, the SO_2 resistance of these catalysts was further evaluated at 225 °C. As can be observed from Fig. 1b, the activity of $MnFeO_x$ (MF) and doped catalysts all experienced a dramatical decrease following the introduction of SO_2 into the feed gas. After the addition of SO_2 for 8 h, the NO conversion of all catalysts fell to less than 75 %, with a continuing downward trend. Although the doping of elements W, Ni, and Co showed some improvement in the SO_2 resistance of the catalysts, it was still insufficient to maintain the long-term stability of the catalysts in SO_2-containing flue gas condition, thus limiting their practical industrial applications.

The best performing catalysts $NiMnFeO_x$ (NMFS) and $WMnFeO_x$ (WMFS) catalysts were then subject to $MnSO_4$ coating method with aim to further improve the SO_2 resistance. Fig. 1c shows the SO_2 resistance result of the $NiMnFeO_x$ (NMFS) and $WMnFeO_x$ (WMFS) catalysts with $MnSO_4$ surface-coated layer. The performance of the corresponding uncoated catalysts is also included in the figure for comparison. As can be seen, both WMFS and NMFS catalysts treated with $MnSO_4$ coating showed outstanding SO_2 resistance and the NO conversion remains stable upon the 8-hour SO_2 poisoning experiment. Notably, compared with the uncoated catalyst, the NO conversion of both catalysts in the absence of SO_2 dropped to some degree, which may be due to a decrease in the number of exposed active sites as compared to the pristine catalyst. Meanwhile, the NMFS exhibits higher activity than WMFS, maintaining a NO conversion of approximately 85 % throughout the 8 hr testing period. Therefore, the NMFS catalyst was selected for further investigation because of its superior performance. Fig. 1d presents the activity of NMFS catalysts with various $MnSO_4$ loading (3–15 wt%), and it is evident that only the catalyst with a 10 wt% $MnSO_4$ loading exhibited robust SO_2 resistance and stability. When the $MnSO_4$ loading was relatively low (3–7 wt%), the $MnSO_4$ coating was insufficient to protect the active metals in the catalyst from sulfidation. As a result, the catalyst experienced a deactivation trend due to the poisoning effect of SO_2. Conversely, when the $MnSO_4$ loading was excessively high ($\geq$ 15 wt%), the $MnSO_4$ layer might overly cover the active sites, leading to a substantial decline in catalyst activity even before the flow-through of SO_2 (below 40 %). Therefore, attaining an appropriate thickness of the $MnSO_4$ coating layer is critical in achieving both good catalytic activity and satisfactory SO_2 resistance. The performance of the catalyst is optimized when the $MnSO_4$ loading is precisely tailored, ensuring that the active metals are sufficiently protected without being overly covered by the $MnSO_4$ layer.

The NMFS catalyst (10 wt% coating $MnSO_4$) with the best SO_2 resistance was further evaluated. The activity and N_2 selectivity of the NMFS catalyst at different temperatures are depicted in Fig. 1e. The NMFS catalyst demonstrated excellent catalytic activity and N_2 selectivity, achieving a NO conversion of over 85 % at above 200 °C and the N_2 selectivity above 90 %. Water vapor present in the flue gas is another detrimental factor to deactivate the catalyst. Hence, long-term stability tests under the co-poisoning of H_2O/SO_2 were also conducted on the NMFS catalyst. As shown in Fig. 1f, the activity of the catalyst was essentially unaffected under conditions where H_2O and SO_2 were individually present. When H_2O and SO_2 were introduced into the reaction gas simultaneously, the activity of the catalyst declined slightly. However, it still maintained a good catalytic activity at about 80 % NO conversion in the following 14 h of reaction, confirming the outstanding stability of the NMFS catalyst under the combined poisoning effects of H_2O and SO_2. The N_2 selectivity under various conditions with the addition of H_2O and SO_2 was also assessed. As shown in Fig. S2a, the NMFS catalyst consistently exhibited good N_2 selectivity (>80 %) when subject to different conditions. Moreover, the time-on-stream (TOS) stability assessment of the NMFS catalyst at 225 °C also indicates that the NMFS catalyst can maintain long-term catalytic stability, regardless of the presence of SO_2 (Fig. S2b-c). These favorable attributes make the NMFS catalyst a highly promising candidate for practical industrial applications, particularly in environments with the presence of both H_2O and SO_2.

3.2. N_2-physisorption and XRD results

All catalysts exhibited typical type IV isotherm curves with narrow hysteresis loops from N_2 physisorption results (Fig. 2a), indicating the predominant presence of mesopores in these samples. The postfix notation of -U indicates used catalyst after the SO_2 poisoning tests. The effect of Ni doping on the specific surface area (S_{bet}) of the catalysts was found to be negligible, with a surface area of 88 m^2/g for the $MnFeO_x$ (MF) catalyst as compared to 91 m^2/g for the $NiMnFeO_x$ (NMF) catalyst. However, the specific surface area of NMFS exhibited a slight decline (from 91 m^2/g to 79 m^2/g when compared to the NMF sample). This decrease of surface area after $MnSO_4$ coating can be attributed to partial blockage of micro- and/or meso-pores of catalyst by non-porous $MnSO_4$ coating layer, which consequently leads to an overall reduction in the average specific surface area of the NMFS catalyst. Simultaneously, based on the Barrett−Joyner−Halenda (BJH) pore size distribution of the catalysts shown in Fig. S3, it can be observed that some pores in the 2–8 nm range have decreased following the introduction of the $MnSO_4$ coating layer. This implies that the $MnSO_4$ surface coating process may contribute to the blockage of mesopores in the NMF catalyst, culminating in a reduced specific surface area for the NMFS catalyst. Following the SO_2 poisoning test, the specific surface area of all catalysts declined, signifying the structural damage to the catalysts due to SO_2 poisoning. However, among the used catalysts, the specific surface area of the NMFS catalyst was the highest and encountered the least decline, suggesting that it was least impacted by the detrimental effects of SO_2, which underscores the superior structural stability and SO_2 resistance of the NMFS catalyst. The BJH pore size distribution offers a detailed perspective on pore size alterations following the SO_2 poisoning test (Fig. S3). For the MF catalyst, there is a decline in pores across all size ranges post-test, suggesting more pronounced poisoning effects. In contrast, the NMF catalyst primarily shows a reduction in the smaller pore size range (2–5 nm). Simultaneously, the emergence of new pores within the 10 nm range results in an augmented pore volume in this particular range. The NMFS catalyst manifests a comparable pattern. However, a notable distinction is the minimal decrease of pores in the smaller pore size range, alluding to the superior structural stability of the NMFS catalyst during the SO_2 poisoning process.

The crystal structures of the catalysts before and after the SO_2 poisoning test were further analysed by XRD and results are shown in Fig. 2b-d. The XRD patterns of all the catalysts remains largely unchanged after reaction, indicating that the SO_2 poisoning reaction did not cause a severe structural collapse of the catalysts. However, it was

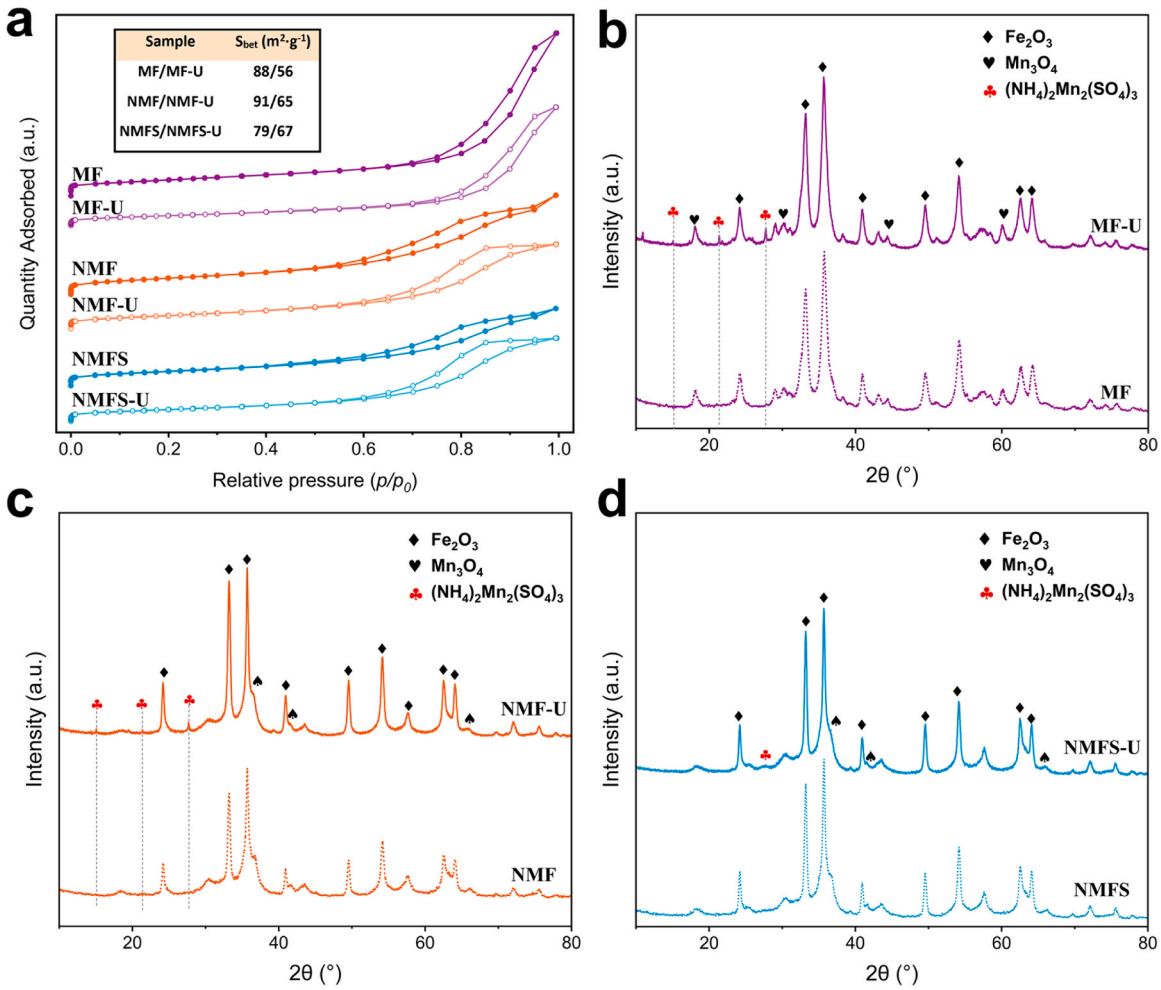

Fig. 2. N_2 adsorption-desorption isotherms (a) and the corresponding BET surface area (inset), and XRD patterns (b-d) of catalysts before/after SO_2 poisoning test. MF, NMF, and NMFS stand for the $MnFeO_x$, $NiMnFeO_x$, and $MnSO_4$-coated $NiMnFeO_x$ catalysts, respectively. Samples with postfix "-U" represent the catalysts after the SO_2 poisoning experiment.

noted that $(NH_4)_2Mn_2(SO_4)_3$ crystals (PDF 04–011–9560) had evidently formed at 15.0°, 21.5°, and 27.7° on both the MF and NMF catalysts after the reaction. The formation of $(NH_4)_2Mn_2(SO_4)_3$ signifies the sulfation of MnO_x in the catalyst due to the reaction with SO_2, which is the primary active substance in the catalysts. The sulfation of the active species will directly result in a decline in the activity of the catalysts. Furthermore, the presence of $(NH_4)_2Mn_2(SO_4)_3$ suggests extensive accumulation of this by-product on the catalyst surface, covering the active sites on the catalyst surface and causing further reduction in catalyst activity. This explains the rapid deactivation of the MF and NMF catalysts in the SO_2 poisoning test. In contrast, a comparison of the XRD patterns of NMFS before and after the SO_2 poisoning test showed that the post-reaction catalyst only exhibited a tiny peak of $(NH_4)_2Mn_2(SO_4)_3$ at $2\theta = 27.7°$. It is worth noting the intensity of this peak is significantly lower than that of the other two catalysts. This indicates that the NMFS catalyst was minimally affected by SO_2 in the reaction, exhibiting weak sulfation of the active metals in the catalyst, thereby maintaining good activity under SO_2 poisoning. This observation is consistent with the results from the activity test (Fig. 1c) and N_2-physisorption experiments (Fig. 2a). It is also noteworthy that the XRD patterns of the NMFS and NMF catalysts are identical, with no $MnSO_4$ crystal peaks detected on the NMFS catalyst. This suggested that the $MnSO_4$ coating layer in the NMFS catalyst is in an amorphous state. This also confirms that NMF and NMFS have similar structures and morphologies, which can be validated by their SEM images as shown in Fig. S4.

3.3. SEM/EDS mapping and thermogravimetric analysis

Consistent with the XRD results, the EDS mapping results also shows that the S element is evenly distributed on the surface of the NMFS catalyst, and no aggregated S were observed (Fig. 3a). The TG curves of the catalysts before and after the SO_2 poisoning test are then compared and shown in Fig. 3b-d. It is evident that the weight loss of the MF-U and NMF-U are more pronounced after the reaction at 4.6 wt% and 4.8 wt%, respectively (Fig. 3b-c). The main weight loss peak of the catalyst after the reaction occurs at around 750 °C, corresponding to the decomposition of manganese sulphate ($MnSO_4$) [31,32]. This indicates that the active MnO_x in the MF and NMF catalysts was largely sulphated to formation of $MnSO_4$, consistent with the XRD results. On the other hand, the weight loss peak at 750 °C can be observed in both NMFS and NMFS-U catalysts, which is from the decomposition of the $MnSO_4$ coating layer in the fresh NMFS catalyst. Compared with the MF and NMF catalysts, the NMFS catalyst before and after the reaction demonstrates a mere 1.4 wt% difference in weight loss. This suggests that the MnO_x in the NMFS catalyst exhibited minimal reactivity with SO_2, consequently least amount of sulphate by-product being formed. These results are consistent with the catalyst performance results, highlighting the excellent SO_2 resistance of the NMFS catalyst.

3.4. EDS and ICP analysis: quantitative analysis of S

To probe the generation of sulphate by-products during the reaction

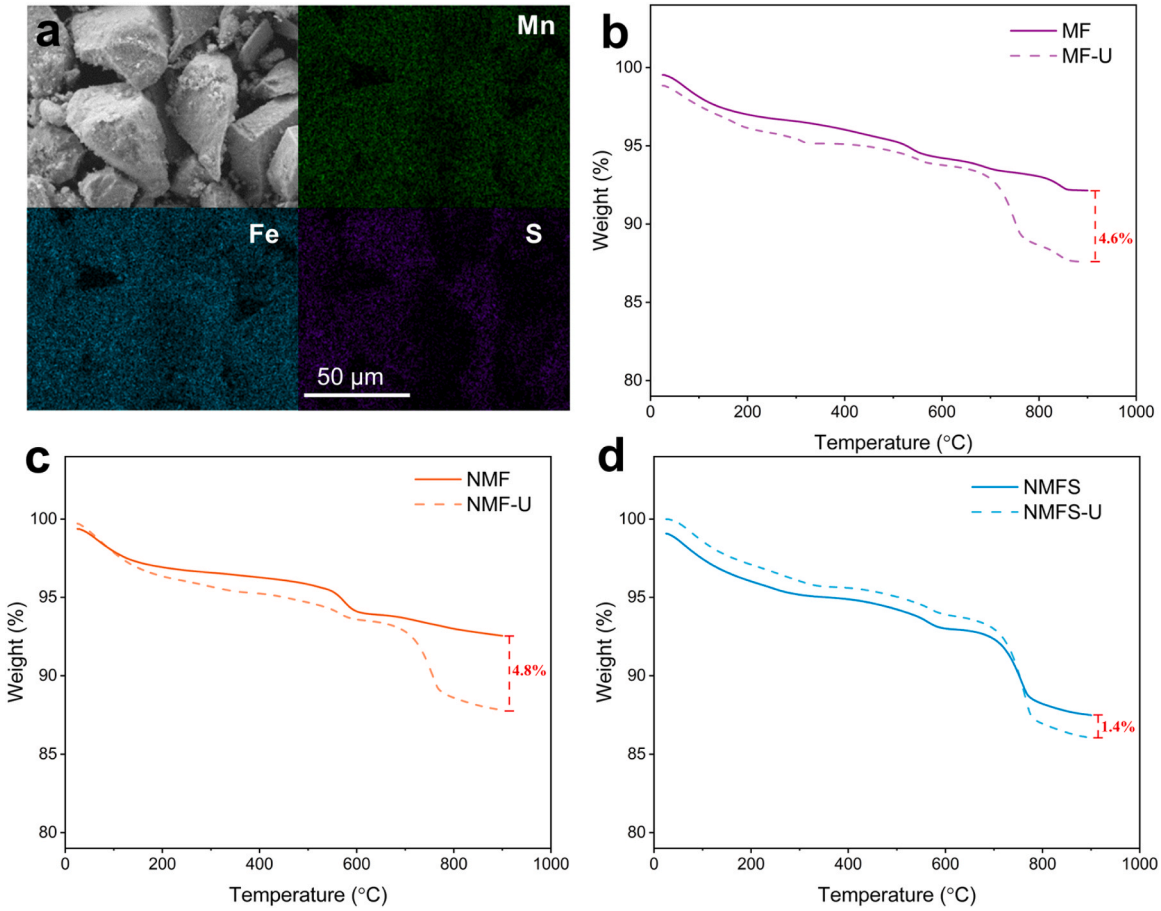

Fig. 3. (a) EDS mapping of elements in the NMFS catalyst. TG curves for the MF (b), NMF (c), and NMFS (d) catalysts before and after the reaction.

between SO_2 and the catalysts, EDS and ICP studies were utilized to quantitatively compare the S content of the three catalysts before and after the reaction. Firstly, as presented in Fig. 4, it can be distinctly observed that both the EDS and ICP results affirm the least increase in S content in the NMFS catalyst after the reaction, confirming the superior SO_2 resistance of $MnSO_4$ coated catalyst, which solidly supports the conclusions drawn in the prior sections. However, a notable discrepancy in S deposition was observed in the MF catalyst between two methods. It is a well-established fact that the EDS technique can only detect the elemental concentration on the surface of the catalyst, whereas ICP measures the overall elemental content within the bulk catalyst. In the case of the MF catalyst, the S increment detected by ICP (1.83 wt%) surpassed twice the amount determined by EDS (0.90 wt%). This discrepancy suggests that a large amount of sulphate is distributed inside the MF catalyst after the reaction, confirming that SO_2-induced active metal sulfation permeates deep within the MF catalyst. In contrast, the increment in S content in the NMF catalyst after the reaction, as detected by both EDS (1.60 wt%) and ICP (1.63 wt%), is almost identical. This implies that Ni doping serves as an effective barrier to SO_2 diffusion within the catalyst, subsequently inhibiting further catalyst poisoning by SO_2. This explains the lower total S increase of the NMF catalyst after the reaction, and the better SO_2 resistance of NMF in the activity test.

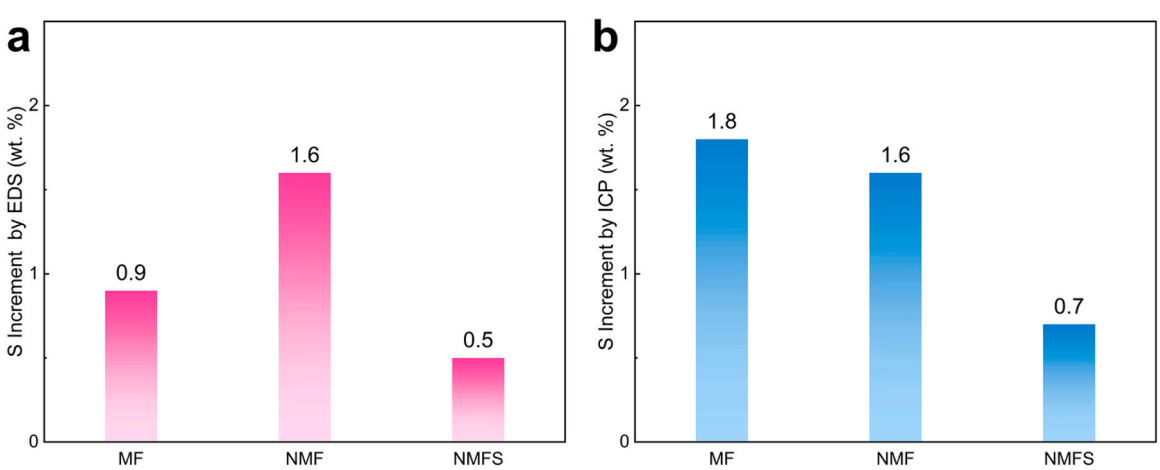

Fig. 4. Increment of S after the SO_2 poisoning reaction detected by EDS (a) and ICP (b) for the catalysts.

Building on this, the NMFS catalyst provides an additional protective $MnSO_4$ coating layer on the surface of the catalyst, thereby achieving a dual protection objective of inhibiting both surface adsorption and internal diffusion of SO_2. As a result, the NMFS catalyst exhibits exceptional SO_2 resistance and outstanding performance in mitigating SO_2 induced catalyst deactivation.

3.5. XPS and XANES results: valence state analysis

The conclusions discussed in the previous section are further supported by the XPS results (Fig. 5). XPS is a surface-sensitive quantitative spectroscopic technique that allows for quantifying the surface S increment of the catalysts during the reaction. As shown in Fig. 5a, the quantitative results from XPS are consistent with those from EDS, where the NMFS catalyst displays the smallest increment in S, while the NMF has the highest surface S increment. Furthermore, the rise in surface nitrogen content after the reaction, which indicates the deposition of nitrate or ammonium sulphate, is also quantified. It can be observed that the NMFS had the lowest post treatment N content, further confirming the superior stability and SO_2 resistance of the NMFS.

The valence states of the main active metal Mn before and after the reaction in the catalyst were further analysed using high-resolution XPS spectra. The atomic proportion of Mn^{2+} and Mn^{3+} can be determined from the fitting results of the Mn 2p spectra [3,33,34]. It can be observed from Fig. 5b-d that, following the SO_2 poisoning reaction, there is a notable increase in the proportion of Mn^{2+} across all catalysts. This indicates that SO_2 poisoning will reduce the Mn species in the catalyst to a lower valence state, which aligns with previous research [35,36]. Notably, Mn with a higher valence state has higher reactivity in the SCR reaction at lower temperatures [37]. Therefore, the reduction of active Mn to a lower valence state could also be a reason for the catalyst deactivation caused by SO_2 poisoning. The normalized XPS fitting results for Mn^{2+} increment after SO_2 poisoning show that the NMF catalyst exhibits the most significant increase in Mn^{2+} after the reaction. This is consistent with the earlier conjecture that the surface of NMF experienced the most severe sulfation among the three catalyst samples (Fig. 4a). In contrast, both MF and NMFS showed smaller increases in Mn^{2+} after the SO_2 poisoning reaction, which is in line with the surface S deposition results derived from XPS analysis (Fig. 5a). However, the XPS fitting results of Mn 2p did not reveal any significant differences between MF and NMFS. This might be attributed to the complexity of the system, which makes XPS fitting challenging and thus makes it difficult to pinpoint any minor distinctions between the two samples.

Given that the XPS technique only measures the Mn on the surface (<10 nm) rather than the bulk catalyst, XANES results were utilized to further analyse the valence state of Mn throughout the entire bulk catalyst. Firstly, as depicted in Fig. 6a, the Mn K-edge positions of NMF and NMFS catalysts are higher than that of the MF catalyst, suggesting a higher valence state of Mn and thus indicating their superior catalytic activity. Following the SO_2 poisoning reaction, both the MF and NMF catalysts displayed a negative shift in their Mn K-edge positions (Fig. 6b-c), indicative of a decrease in the Mn valence state, which is consistent with the XPS findings. However, divergent from the XPS results, the peak shift of the NMF catalyst is less pronounced than that of the MF

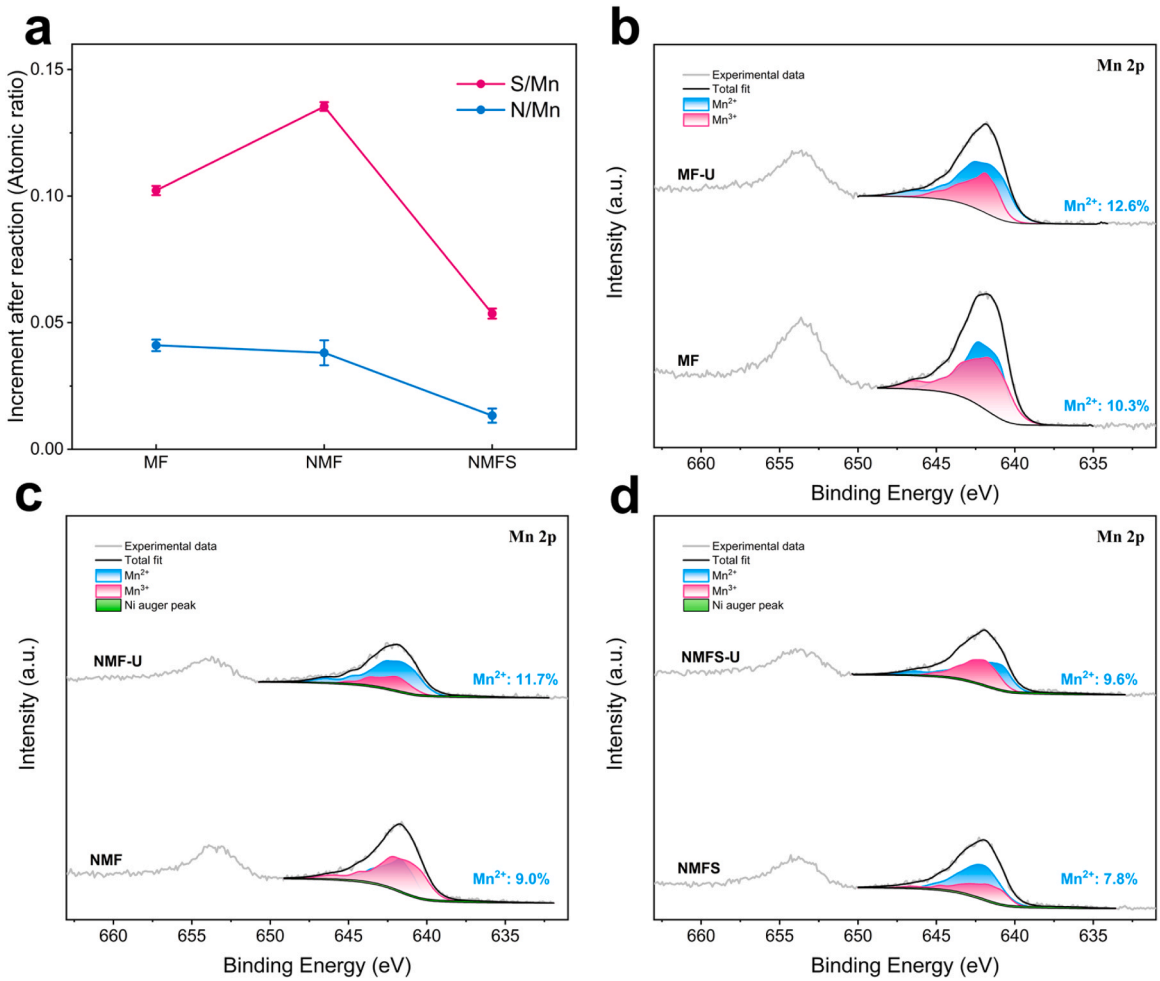

Fig. 5. (a) S and N increment caused by the SO_2 poisoning reaction, determined from difference in atomic ratio (element/Mn) before and after processing. Atomic percentage of Mn^{2+} in fresh MF (b), NMF (c), and NMFS (d) catalysts and their corresponding catalysts after SO_2 poisoning tests (MF-U, NMF-U, NMFS-U).

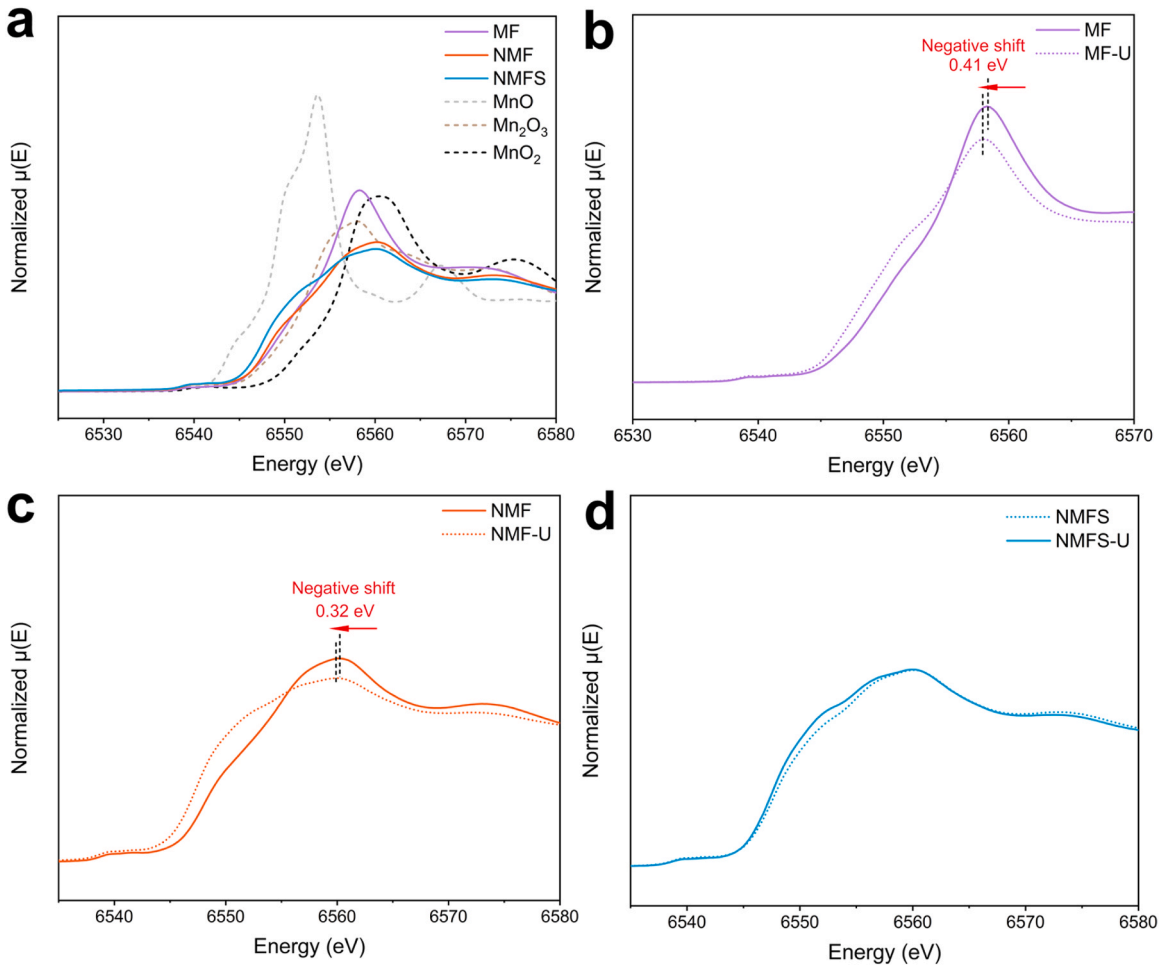

Fig. 6. Mn K-edge XANES spectra of fresh catalysts and manganese oxide standards (a), and comparison of the catalysts before/after SO_2 poisoning reaction (b-d).

catalyst. This suggests that the overall valence state of the Mn species within the NMF catalyst underwent a less substantial decrease compared to that in the MF catalyst following the SO_2 poisoning. This valence state discrepancy between surface Mn and overall Mn in the catalysts reinforces the earlier hypothesis that the incorporation of Ni allows the NMF catalyst to restrict further SO_2 diffusion within the catalyst, thereby safeguarding the internal Mn species from deactivation due to the SO_2 poisoning. This protection offered by Ni doping contributes to the enhanced SO_2 resistance and stability of the NMF catalyst.

By contrast, as shown in Fig. 6d, the position and intensity of the Mn K-edge in the NMFS catalyst exhibit minimal changes before and after the reaction. This observation attests to the fact that the Mn species within the NMFS catalyst maintain their valence state, even after exposing to SO_2. This stability is a crucial factor in the exceptional resistance of the NMFS catalyst towards SO_2-induced deactivation. The protective $MnSO_4$ coating layer on the surface of the NMFS catalyst effectively prevents the reaction with SO_2, thereby maintaining the stability and activity of the catalyst.

3.6. H_2-TPR results and in-situ DRIFTS study

The influence of SO_2 poisoning on the characteristics of the catalyst

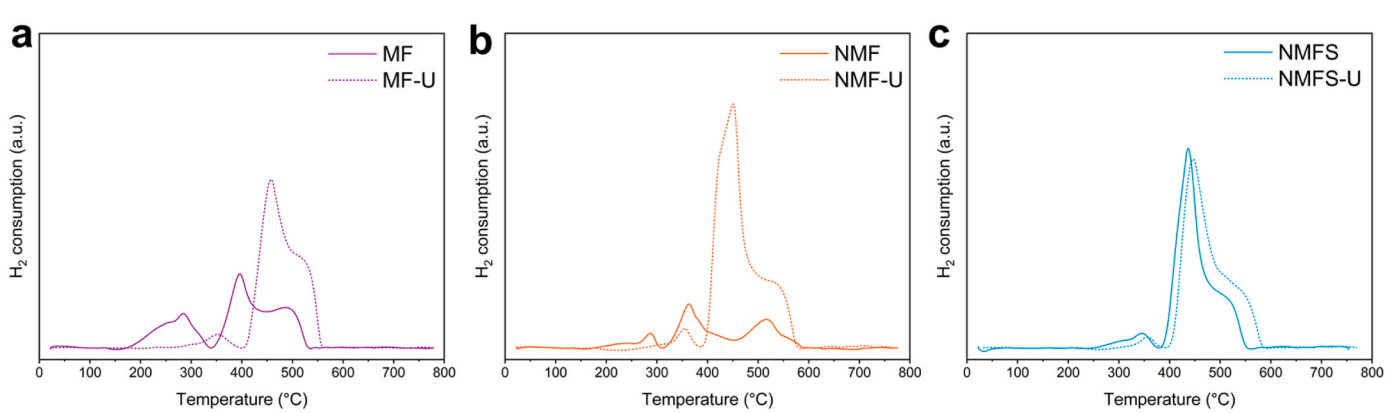

Fig. 7. H_2-TPR profiles of MF (a), NMF, NMFS catalysts and their respective post-reaction catalysts.

is further investigated employing H_2-TPR experiments, as shown in Fig. 7. Upon comparing the H_2-TPR results of the catalysts before and after the reaction, it can be observed that a newly generated peak within the 400–500 °C range emerges as the dominant peak for both the MF and NMF catalysts after the reaction, which correlates with the reduction of $MnSO_4$ [38,39]. This implies that the catalysts have reacted with SO_2 and produced a significant amount of $MnSO_4$ during the SO_2 poisoning reaction, which also explains their rapid deactivation observed in both the MF and NMF catalysts during the SO_2 poisoning process. In contrast, for the NMFS catalyst, there is minimal alteration in the H_2-TPR curves after the SO_2 poisoning test. The dominant peak within 400–500 °C originates from the reduction of the $MnSO_4$ coating layer, and its positions and areas remain unvaried after the reaction. This denotes that virtually no new $MnSO_4$ species were generated in the NMFS catalyst during the SO_2 poisoning reaction. This further substantiates that the protective $MnSO_4$ coating layer in the NMFS catalyst can effectively prevent the reaction of MnO_x with SO_2, preserving the activity of the catalyst in the presence of SO_2.

Concurrently, from the H_2-TPR profiles of the fresh catalysts, it is noticeable that the reduction peaks of the MF and NMF catalysts are more pronounced in comparison to NMFS, indicating their higher reactivity under reductive conditions. Generally, this characteristic is beneficial for the performance of the SCR catalysts. However, it also implies a greater likelihood for these catalysts to react with the reductive gas SO_2 and consequently become deactivated. In contrast, the NMFS catalyst exhibits lesser activity under reductive conditions and thus, is less susceptible to deactivation by reaction with SO_2.

Subsequently, in situ DRIFTS experiments were utilized to explore the adsorption properties of the catalyst towards SO_2 to substantiate the aforementioned conclusions. As shown in Fig. 8, the band at 1615–1618 cm^{-1} is ascribed to H_2O, resulting from the reaction between SO_2 and the surface basic hydroxyls [40,41]. Within the 60 min following the introduction of SO_2 to the feed gas, the intensity of this peak rapidly escalates on the surface of the NMF catalyst (Fig. 8a), implying a robust adsorption reaction of SO_2 on the catalyst surface. In contrast, the rise in the corresponding peak at 1615 cm^{-1} over time on the NMFS catalyst is rather modest (Fig. 8b), indicating weak adsorption of SO_2 on the NMFS surface. Simultaneously, the peaks corresponding to surface sulphates exhibit analogous trends, confirming the relatively weaker adsorption of SO_2 on the surface of the NMFS. Within 60 min of SO_2 interacting with the catalysts, the peaks corresponding to the surface sulphate species (1272 cm^{-1},1213 cm^{-1}, and 1152 cm^{-1}) formed rapidly escalate on the NMF catalyst, with an intensity significantly surpassing the surface sulphate peaks (1228 cm^{-1} and 1051 cm^{-1}) on the NMFS catalyst surface [36,41–45]. These results provide further validation of the protective role of the $MnSO_4$ coating layer on the catalyst surface against SO_2 poisoning, reinforcing the excellent SO_2 resistance of the NMFS catalyst.

3.7. Synchrotron EXAFS analysis and DFT calculations

To further substantiate the experimental conclusions from a theoretical standpoint, DFT calculations were employed. Accurate and sensible catalyst structural configurations are critical in obtaining meaningful results from DFT calculations. Hence, the actual structures of the catalysts were first established based on the results derived from synchrotron EXAFS experimental results. The Fourier transform EXAFS (FT-EXAFS) spectra of the Mn K-edge for the catalysts and Mn oxide/foil standards, are depicted in Fig. 9a. Peaks located at 1–2 Å in R space, which are associated with the first shell of Mn-O scattering, can be observed in all catalysts. Concurrently, peaks seen at 2–3 Å originate from Mn and its surrounding coordination metal atoms, which aligns with the characteristic of mixed oxide catalysts. It is notable that the FT-EXAFS spectra of the NMF and NMFS catalysts demonstrate high similarity, attesting that the $MnSO_4$ layer coating process will not alter the structure of the catalyst. This structural resemblance between the NMF and NMFS catalysts is further corroborated by the Mn K-edge wavelet transform-EXAFS (WT-EXAFS) (Fig. 9b). Furthermore, by comparing the WT-EXAFS spectra of the catalysts before and after the reaction, it can be seen that the structures of both NMF and NMFS catalysts do not significantly change after the SO_2 poisoning reaction, underscoring their structural stability during the reaction. Consequently, EXAFS fitting was carried out on the NMF catalyst to determine the fine structural configuration of the catalyst (Fig. 9c), and the detailed fitting results are provided in Table S1. Based on the fitting results, a model of the NMF catalyst was constructed and presented in Fig. 9d. The structure of the NMFS catalyst was established by adsorbing $MnSO_4$ onto the surface of the NMF catalyst. The constructed catalyst models were further optimized by DFT calculations to achieve the configuration with the lowest energy. The catalyst structures after the reaction (NMF-U and NMFS-U) were constructed in the same way by adsorbing SO_2 onto the surface of the fresh catalyst.

Based on the constructed models of the SO_2-adsorbed catalysts, the adsorption energy of SO_2 on the surfaces of both NMF and NMFS catalysts is calculated and presented in Fig. 10a. It is evident that the adsorption of SO_2 on the surface of the NMFS catalyst is substantially weaker than that on the NMF catalyst, which aligns with the in situ DRIFTS results. This reaffirms that the $MnSO_4$ coating layer can

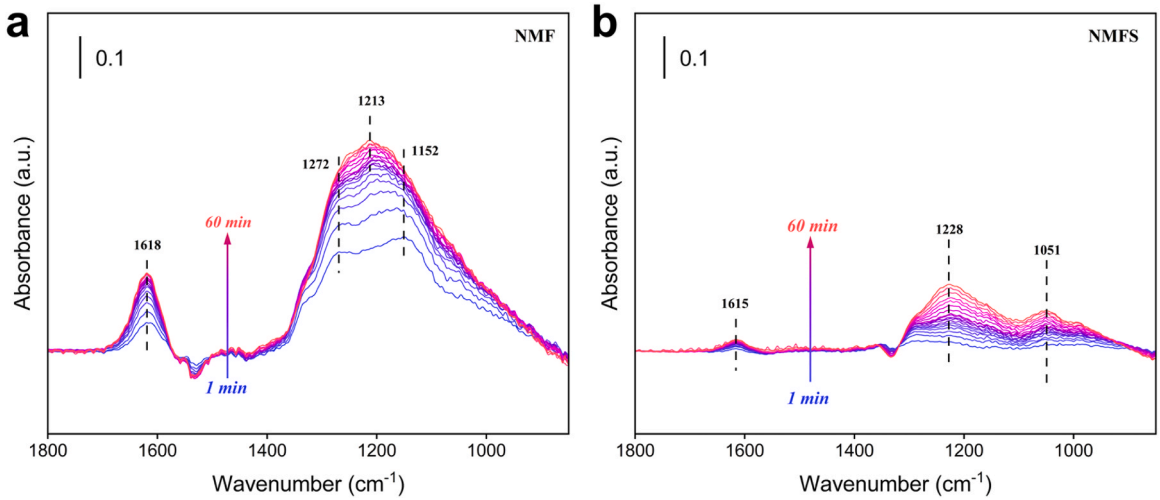

Fig. 8. *In situ* DRIFTS spectra obtained over (a) NMF and (b) NMFS catalysts following a 60-min SO_2 exposure test. Reaction condition: 200 ppm SO_2 + 3 % O_2, balanced with N_2. GHSV= 60,000 h^{-1} at a temperature of 225 °C.

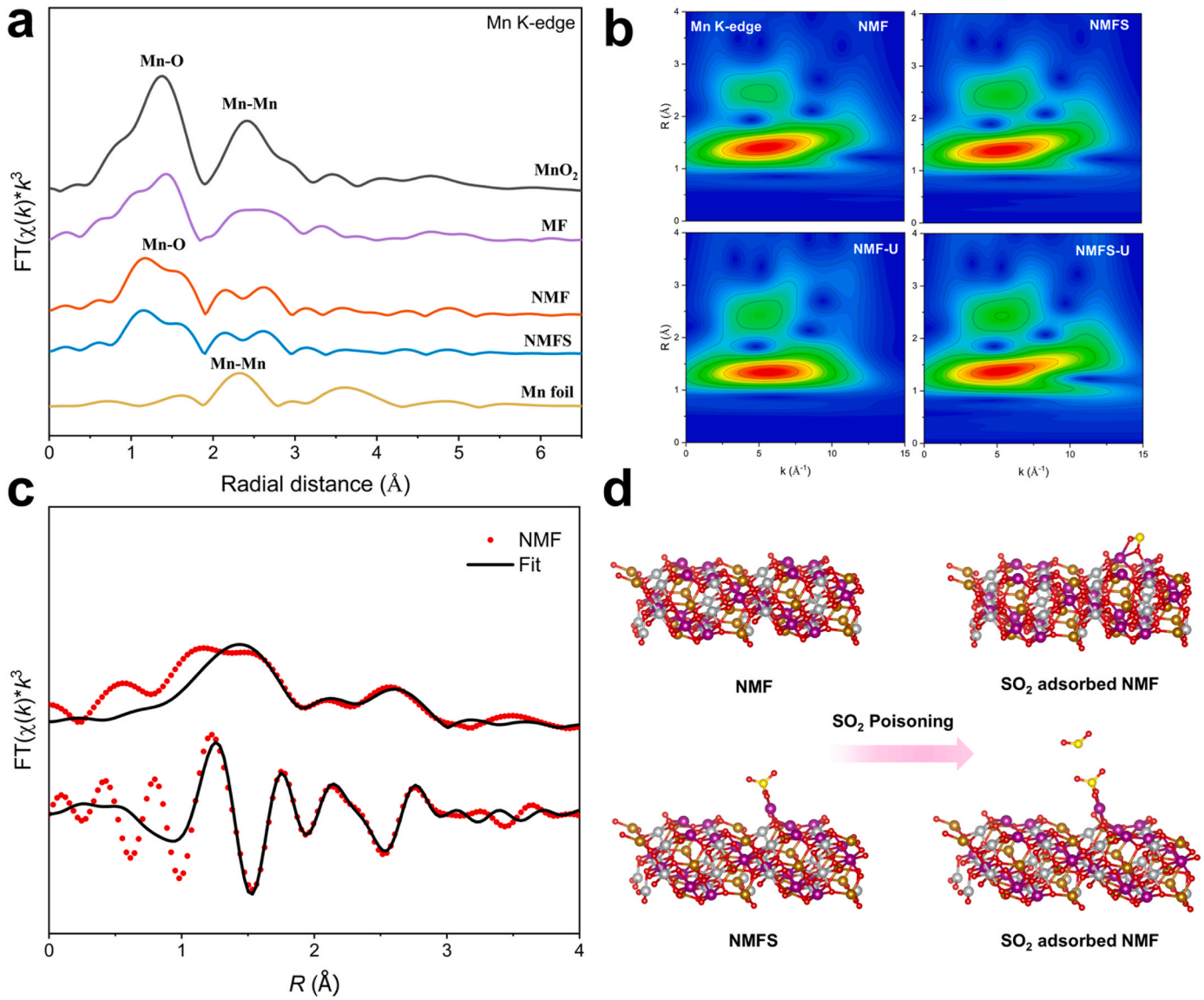

Fig. 9. (a) k^3-weighted FT of Mn K-edge EXAFS for the catalysts and Mn foils/oxide. (b) Mn K-edge WT-EXAFS spectra of NMF, NMFS and the corresponding post-reaction catalysts. (c) Mn K-edge EXAFS (points) and curve fit (line) for NMF catalyst, shown in R-space (FT magnitude and imaginary component, k^3-weighted). (d) Structural configurations of the NMF, NMFS, NMF-U, and NMFS-U catalysts after DFT structural optimization. Red, yellow, brown, purple, and gray spheres represent O, S, Fe, Mn, and Ni atoms, respectively.

effectively inhibit the adsorption of SO_2 on the NMFS catalyst surface, thereby enhancing the SO_2 resistance of the NMFS catalyst, corroborating our experimental results. Subsequently, the electron localization function (ELF) calculations are conducted to analyse the superior SO_2 resistance of the NMFS catalyst from the perspective of electronic structure. As depicted in Fig. 10b, a significant electronic redistribution of Mn in the NMF catalyst is observed after SO_2 adsorption. The free electrons around Mn are transferred to SO_2 molecule following the adsorption, indicative of a strong ionic bond between Mn and the adsorbed SO_2. For the NMFS catalyst, a similar enhancement of electron localization can also be observed around Mn atoms following SO_2 adsorption, indicating that the adsorption of SO_2 still exerts some influence on the NMFS catalyst. However, due to the shielding effect of the $MnSO_4$ coating layer on the surface, the charge redistribution occurs solely within the NMFS catalyst, preventing any charge transfer between the adsorbed SO_2 and the catalyst. This observation is further validated by Bader charge calculations. As shown in Fig. 10c, the charge transfer between SO_2 and the catalyst in NMFS-U (0.01 e), is evidently lower than that in the NMF-U catalyst (0.69 e), signalling a reduced level of influence from SO_2 on the Mn in the catalyst. The VCDD maps in Fig. 10c provide a more intuitive display of the charge difference caused by SO_2 adsorption. While SO_2 adsorption does lead to some alterations in the charge distribution of the NMFS catalyst, there is no substantial charge exchange and interaction between SO_2 and the NMFS catalyst, as is observed with the NMF catalyst. This reiterates the weaker interaction between SO_2 and the NMFS catalyst.

The mechanism underlying the superior SO_2 resistance of the NMFS catalyst can be further elucidated via PDOS results. As revealed in Fig. 10d, the Mn 3d orbitals of the NMFS catalyst display a stark contrast with those of the NMF catalyst. The D-band centre of Mn in the NMF catalyst is substantially elevated compared to that in the NMFS catalyst when benchmarked against the Fermi level. As per the D-band centre theory proposed by Nørskov et al., this suggests that Mn in NMF exhibits a stronger adsorptive capability for SO_2 [46]. Upon SO_2 adsorption on narrow valence bands (d band), the adsorbate state will split into localized bonding and antibonding states. A higher D-band centre implies that more antibonding orbitals are situated above the Fermi level, thereby not being filled by electrons. This results in a decreased

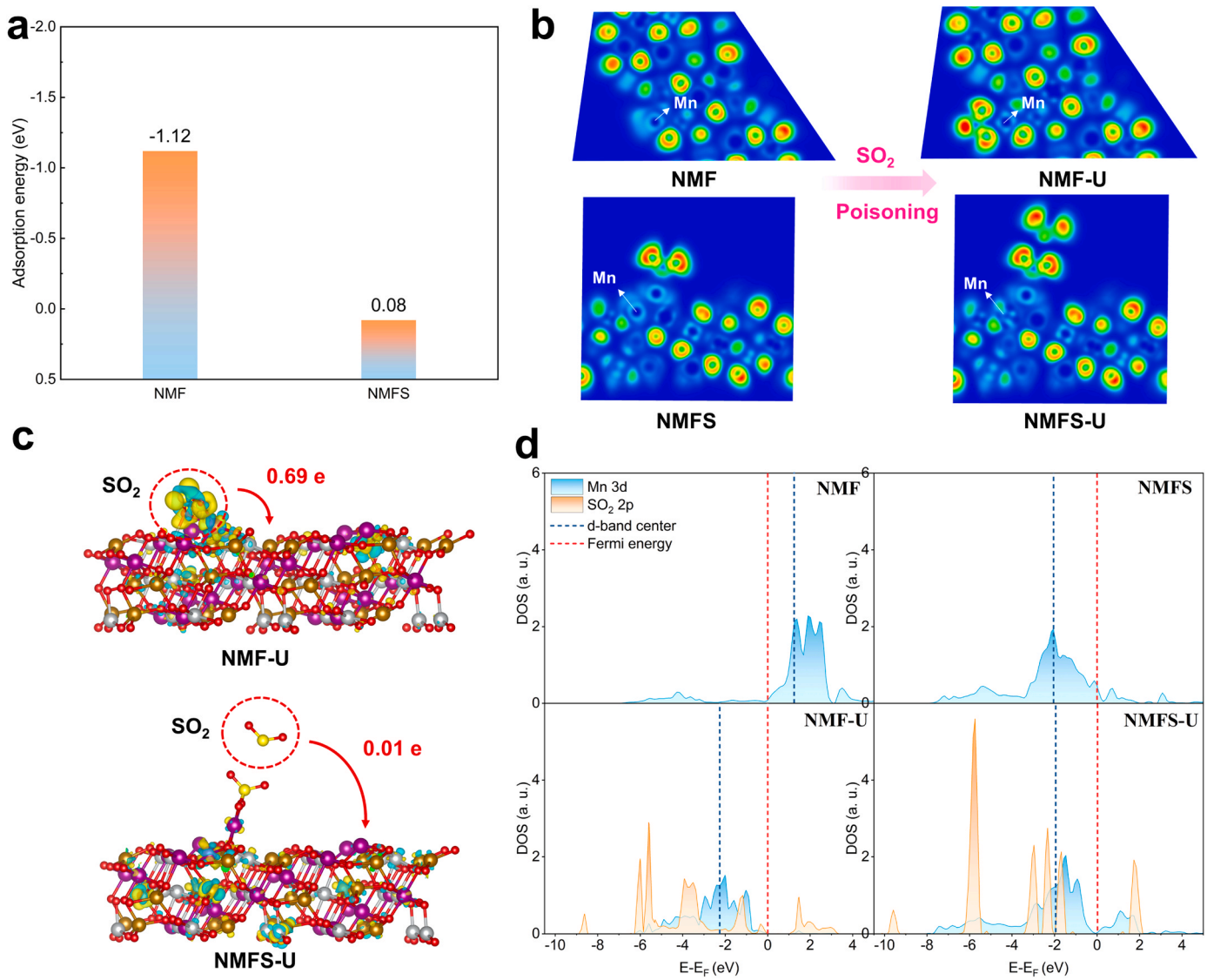

Fig. 10. (a) The calculated adsorption energy of SO_2 on the NMF and NMFS catalysts. (b) ELF maps of NMF, NMFS, and post-reaction NMF-U and NMFS-U catalysts. (c) VCDD maps and Bader charge results of the SO_2-adsorbed NMF and NMFS catalysts. The blue regions represent charge depletion, whereas the yellow regions signify charge accumulation. (d) PDOS for Mn 3d and SO_2 2p orbitals of the catalysts and the adsorbed SO_2 molecule. The D-band centre of Mn is indicated by the blue dashed line.

influence of antibonding orbitals on bonding, thus stabilizing the adsorption of adsorbate. Thus, based on the position of the D-band centre, it can be concluded that the NMF catalyst exhibits a stronger adsorption capacity for SO_2 when compared to the NMFS catalyst. Furthermore, the PDOS of Mn 3d orbitals in the NMF-U catalyst demonstrate a crucial change in contrast to the fresh NMF catalyst, indicating the significant influence of SO_2 on the Mn in the NMF catalyst. In contrast, no significant changes are observed in the Mn 3d orbitals of the NMFS catalyst after the SO_2 adsorption, and the D-band centre remains almost unshifted. This suggests that Mn in the NMFS catalyst undergoes negligible changes following the reaction with SO_2, thereby maintaining good activity under the poisoning of SO_2 in the SCR reaction. These results further underscore the superior SO_2 resistance of the NMFS catalyst with the $MnSO_4$ coating layer.

4. Conclusions

This work presents a facile yet effective strategy to enhance the stability and robustness of the Mn-based low-temperature SCR catalysts against SO_2 poisoning. The results indicate that the fabricated $MnSO_4$-coated $NiMnO_x$ (NMFS) catalyst not only exhibits excellent NO conversion activity and N_2 selectivity but also demonstrates exceptional stability when subjected to the challenging co-poisoning conditions of H_2O and SO_2. Compared to the control $MnFeO_x$ (MF) catalyst, the superior SO_2 resistance property is achieved via Ni doping coupled with an additional $MnSO_4$ coating layer, thus ensuring long-term stability under low-temperature reaction conditions in the presence of SO_2. Comprehensive advanced characterizations revealed that the outstanding SO_2 resistance of the NMFS catalyst results from a dual-protection mechanism.

Firstly, based on the characterization results, the doping of Ni can mitigate the SO_2 poisoning interior of the catalyst, thus restricting the sulfation of the catalyst to its surface, providing a certain degree of protection to the catalyst during SO_2 poisoning reactions. This might stem from a potential connection between the capability of Ni doping to hinder the diffusion of SO_2 within the catalyst, though additional research is necessary to elucidate the specific mechanism underlying this phenomenon. Secondly, the $NiMnSO_4$ coating layer further safeguards the surface of the Ni-doped $MnFeO_x$ catalyst. It not only significantly curtails the adsorption of SO_2 and the deposition of sulphate on

the surface of the catalyst, but also shields the valence state of the active metal from being impacted by SO_2 poisoning.

The DFT calculation results provide additional supportive information for the experimental conclusions. Specifically, the $NiMnSO_4$ coating layer can modulate the electronic state of the active Mn in the catalyst, which efficaciously obstructs the adsorption of SO_2 on the surface of the catalyst during SO_2 poisoning reactions, thereby enhancing its SO_2 resistance.

This method is cost-effective, yet robust, emphasizing its significant value and transformative potential for industrial applications of low-temperature NH_3-SCR catalysts. This innovative approach also provides a deeper understanding of the underlying mechanisms that contribute to the enhanced SO_2 resistance of the catalysts. The combination of Ni doping and the $MnSO_4$ surface coating represents a promising direction for designing catalysts with superior performance and extended durability in SO_2-rich environments, underscores its substantial value and potential transformative impact for industrial applications of low temperature NH_3-SCR catalysts.

CRediT authorship contribution statement

Shuhao Li: Investigation, Methodology, Formal analysis, and Writing – original draft. **Feng Wang:** Writing – review & editing and Supervision. **Derrick Ng:** Methodology, Writing – review & editing and Supervision. **Qiqi Shi:** Experiments and data analysis (in situ- DRIFTS). **Thomas J. Raeber:** Experiments and data analysis (XPS). **Simon James:** Experiments and data analysis (XAS). **Boxiong Shen:** Resources and Supervision. **Zongli Xie:** Resources, Writing – review & editing and Supervision.

Declaration of Competing Interest

The authors declare that they have no known competing financial interests or personal relationships that could have appeared to influence the work reported in this paper.

Data availability

Data will be made available on request.

Acknowledgement

SL acknowledges the Tuition Fee Scholarship (TFS) from the Swinburne University of Technology. The synchrotron experiment was undertaken on the MEX beamline at the Australian Synchrotron, part of ANSTO (Proposal ID 18797). The project was supported by Joint Funds of the National Natural Science Foundation of China (U20A20302), Project of Great Transformation of Scientific and Technical Research in Hebei Province (21283701Z), Innovative Group Projects in Hebei Province (E2021202006), and CSIRO Manufacturing. Special thanks are given to the Supercomputing Resources provided by the Swinburne University of Technology.

Appendix A. Supporting information

Supplementary data associated with this article can be found in the online version at doi:10.1016/j.apcatb.2023.123441.

References

[1] S. Xie, W. Tan, Y. Li, L. Ma, S.N. Ehrlich, J. Deng, P. Xu, F. Gao, L. Dong, F. Liu, Copper single atom-triggered niobia–ceria catalyst for efficient low-temperature reduction of nitrogen oxides, ACS Catal. 12 (2022) 2441–2453.
[2] W. Yoon, Y. Kim, G. Jong Kim, J.-R. Kim, S. Lee, H. Han, G. Hyeon Park, H.-J. Chae, W. Bae Kim, Boosting low temperature De-NOx performance and SO2 resistance over Ce-doped two dimensional Mn-Cr layered double oxide catalyst, Chem. Eng. J. 434 (2022).
[3] B. Thirupathi, P.G. Smirniotis, Nickel-doped Mn/TiO2 as an efficient catalyst for the low-temperature SCR of NO with NH3: catalytic evaluation and characterizations, J. Catal. 288 (2012) 74–83.
[4] T. Yan, Q. Liu, S. Wang, G. Xu, M. Wu, J. Chen, J. Li, Promoter rather than inhibitor: phosphorus incorporation accelerates the activity of V2O5–WO3/TiO2 catalyst for selective catalytic reduction of NO x by NH3, ACS, Catalysis 10 (2020) 2747–2753.
[5] K. Guo, J. Ji, W. Song, J. Sun, C. Tang, L. Dong, Conquering ammonium bisulfate poison over low-temperature NH3-SCR catalysts: a critical review, Appl. Catal. B Environ. 297 (2021), 120388.
[6] X. Zhou, P. Wang, Z. Shen, S. Chen, Q. Wang, D. Cheng, D. Zhang, Low-temperature NOx reduction over hydrothermally stable SCR catalysts by engineering low-coordinated Mn active sites, Chem. Eng. J. 442 (2022).
[7] L.-g Wei, R.-t Guo, J. Zhou, B. Qin, X. Chen, Z.-x Bi, W.-g Pan, Chemical deactivation and resistance of Mn-based SCR catalysts for NOx removal from stationary sources, Fuel 316 (2022).
[8] G. Xu, X. Guo, X. Cheng, J. Yu, B. Fang, A review of Mn-based catalysts for low-temperature NH 3-SCR: NO x removal and H 2 O/SO 2 resistance, Nanoscale 13 (2021) 7052–7080.
[9] X. Fang, Y. Liu, Y. Cheng, W. Cen, Mechanism of Ce-modified birnessite-MnO2 in promoting SO2 poisoning resistance for low-temperature NH3-SCR, ACS Catal. 11 (2021) 4125–4135.
[10] J. Li, C. Zhang, Q. Li, T. Gao, S. Yu, P. Tan, Q. Fang, G. Chen, Promoting mechanism of SO2 resistance performance by anatase TiO2 {0 0 1} facets on Mn-Ce/TiO2 catalysts during NH3-SCR reaction, Chem. Eng. Sci. 251 (2022).
[11] R. Purbia, S.Y. Choi, H.J. Kim, B. Ye, B. Jeong, D.H. Lee, H. Park, H.-D. Kim, J. M. Baik, Cu- and Ce-promoted nano-heterostructures on vanadate catalysts for low-temperature NH3–SCR activity with improved SO2 and water resistance, Chem. Eng. J. 437 (2022).
[12] J. Chen, P. Fu, D. Lv, Y. Chen, M. Fan, J. Wu, A. Meshram, B. Mu, X. Li, Q. Xia, Unusual positive effect of SO2 on Mn-Ce mixed-oxide catalyst for the SCR reaction of NOx with NH3, Chem. Eng. J. 407 (2021).
[13] D. An, S. Yang, W. Zou, J. Sun, W. Tan, J. Ji, Q. Tong, C. Sun, D. Li, L. Dong, Unraveling the SO2 Poisoning Effect over the Lifetime of MeOx (Me = Ce, Fe, Mn) Catalysts in Low-Temperature NH3-SCR: interaction of reaction atmosphere with surface species, J. Phys. Chem. C 126 (2022) 12168–12177.
[14] Y. Shi, H. Yi, F. Gao, S. Zhao, Z. Xie, X. Tang, Evolution mechanism of transition metal in NH3-SCR reaction over Mn-based bimetallic oxide catalysts: structure-activity relationships, J. Hazard. Mater. 413 (2021), 125361.
[15] F. Wang, B. Shen, S. Zhu, Z. Wang, Promotion of Fe and Co doped Mn-Ce/TiO2 catalysts for low temperature NH3-SCR with SO2 tolerance, Fuel 249 (2019) 54–60.
[16] B. Shen, Y. Wang, F. Wang, T. Liu, The effect of Ce–Zr on NH3-SCR activity over MnOx (0.6)/Ce0. 5Zr0. 5O2 at low temperature, Chem. Eng. J. 236 (2014) 171–180.
[17] Y. Xiong, C. Tang, X. Yao, L. Zhang, L. Li, X. Wang, Y. Deng, F. Gao, L. Dong, Effect of metal ions doping (M= Ti4+, Sn4+) on the catalytic performance of MnOx/CeO2 catalyst for low temperature selective catalytic reduction of NO with NH3, Appl. Catal. A Gen. 495 (2015) 206–216.
[18] B. Shen, X. Zhang, H. Ma, Y. Yao, T. Liu, A comparative study of Mn/CeO2, Mn/ZrO2 and Mn/Ce-ZrO2 for low temperature selective catalytic reduction of NO with NH3 in the presence of SO2 and H2O, J. Environ. Sci. 25 (2013) 791–800.
[19] S. Yang, F. Qi, S. Xiong, H. Dang, Y. Liao, P.K. Wong, J. Li, MnOx supported on Fe–Ti spinel: a novel Mn based low temperature SCR catalyst with a high N2 selectivity, Appl. Catal. B Environ. 181 (2016) 570–580.
[20] L. Jia, J. Liu, D. Huang, J. Zhao, J. Zhang, K. Li, Z. Li, W. Zhu, Z. Zhao, J. Liu, Interface engineering of a bifunctional Cu-SSZ-13@ CZO core–shell catalyst for boosting potassium ion and SO2 tolerance, ACS Catal. 12 (2022) 11281–11293.
[21] Q. Cai, F. Wang, Y. Hou, Y. Jia, B. Liao, B. Shen, D. Zhang, Core-shell materials for selective catalytic reducing of NOx with ammonia: synthesis, anti-poisoning performance, and remaining challenges, Fuel Process. Technol. 243 (2023), 107675.
[22] S. Xiong, Y. Peng, D. Wang, N. Huang, Q. Zhang, S. Yang, J. Chen, J. Li, The role of the Cu dopant on a Mn3O4 spinel SCR catalyst: improvement of low-temperature activity and sulfur resistance, Chem. Eng. J. 387 (2020), 124090.
[23] Z. Liu, G. Sun, C. Chen, K. Sun, L. Zeng, L. Yang, Y. Chen, W. Wang, B. Liu, Y. Lu, Fe-doped Mn3O4 spinel nanoparticles with highly exposed Feoct–O–Mntet sites for efficient selective catalytic reduction (SCR) of NO with ammonia at low temperatures, ACS Catal. 10 (2020) 6803–6809.
[24] C. Wang, F. Gao, S. Ko, H. Liu, H. Yi, X. Tang, Structural control for inhibiting SO2 adsorption in porous MnCe nanowire aerogel catalysts for low-temperature NH3-SCR, Chem. Eng. J. 434 (2022), 134729.
[25] L. Zhang, L. Shi, L. Huang, J. Zhang, R. Gao, D. Zhang, Rational design of high-performance DeNO x catalysts based on Mn x Co3–x O4 nanocages derived from metal–organic frameworks, ACS Catal. 4 (2014) 1753–1763.
[26] W. Yoon, Y. Kim, G.J. Kim, J.-R. Kim, S. Lee, H. Han, G.H. Park, H.-J. Chae, W. B. Kim, Boosting low temperature De-NOx performance and SO2 resistance over Ce-doped two dimensional Mn-Cr layered double oxide catalyst, Chem. Eng. J. 434 (2022), 134676.
[27] D. Ng, D. Acharya, X. Wang, C.D. Easton, J. Wang, Z. Xie, Low temperature SCR of NOx over Mn/Fe mixed oxides catalyst: comparison of synthesis methods, J. Chem. Technol. Biotechnol. 96 (2021) 2681–2695.
[28] B. Ravel, M. Newville, Athena, Artemis, Hephaestus: data analysis for X-ray absorption spectroscopy using IFEFFIT, J. Synchrotron Radiat. 12 (2005) 537–541.
[29] H. Funke, M. Chukalina, A.C. Scheinost, A new FEFF-based wavelet for EXAFS data analysis, J. Synchrotron Radiat. 14 (2007) 426–432.

[30] Y. Zhang, X. Long, X. Liu, G. Chen, N. Zhang, M. Li, R. Ma, H. Wan, Superlattice-like Co-doped Mn Oxide and NiFe hydroxide nanosheets toward an energetic oxygen evolution reaction, ACS Sustain. Chem. Eng. 10 (2022) 5683–5692.
[31] X. An, C. Feng, J. Liu, G. Cheng, Y. Du, Z. Fan, X. Wu, Insight into the sulfur resistance of manganese oxide for NH3-SCR: perspective from the valence state distributions, Appl. Surf. Sci. 592 (2022).
[32] C. Wang, F. Gao, S. Ko, H. Liu, H. Yi, X. Tang, Structural control for inhibiting SO2 adsorption in porous MnCe nanowire aerogel catalysts for low-temperature NH3-SCR, Chem. Eng. J. 434 (2022).
[33] M.C. Biesinger, B.P. Payne, A.P. Grosvenor, L.W. Lau, A.R. Gerson, R.S.C. Smart, Resolving surface chemical states in XPS analysis of first row transition metals, oxides and hydroxides: Cr, Mn, Fe, Co and Ni, Appl. Surf. Sci. 257 (2011) 2717–2730.
[34] B. Thirupathi, P.G. Smirniotis, Co-doping a metal (Cr, Fe, Co, Ni, Cu, Zn, Ce, and Zr) on Mn/TiO2 catalyst and its effect on the selective reduction of NO with NH3 at low-temperatures, Appl. Catal. B Environ. 110 (2011) 195–206.
[35] L. Jiang, Q. Liu, G. Ran, M. Kong, S. Ren, J. Yang, J. Li, V2O5-modified Mn-Ce/AC catalyst with high SO2 tolerance for low-temperature NH3-SCR of NO, Chem. Eng. J. 370 (2019) 810–821.
[36] Z. Chen, S. Ren, M. Wang, J. Yang, L. Chen, W. Liu, Q. Liu, B. Su, Insights into samarium doping effects on catalytic activity and SO2 tolerance of MnFeO catalyst for low-temperature NH3-SCR reaction, Fuel 321 (2022).
[37] P. Sun, S.-x Huang, R.-t Guo, M.-y Li, S.-m Liu, W.-g Pan, Z.-g Fu, S.-w Liu, X. Sun, J. Liu, The enhanced SCR performance and SO2 resistance of Mn/TiO2 catalyst by the modification with Nb: a mechanistic study, Appl. Surf. Sci. 447 (2018) 479–488.
[38] L. Ma, J. Li, R. Ke, L. Fu, Catalytic performance, characterization, and mechanism study of Fe2 (SO4) 3/TiO2 catalyst for selective catalytic reduction of NOx by ammonia, J. Phys. Chem. C 115 (2011) 7603–7612.
[39] B. Thirupathi, P.G. Smirniotis, Effect of nickel as dopant in Mn/TiO 2 catalysts for the low-temperature selective reduction of NO with NH 3, Catal. Lett. 141 (2011) 1399–1404.
[40] C. Sun, W. Chen, X. Jia, A. Liu, F. Gao, S. Feng, L. Dong, Comprehensive understanding of the superior performance of Sm-modified Fe2O3 catalysts with regard to NO conversion and H2O/SO2 resistance in the NH3-SCR reaction, Chin. J. Catal. 42 (2021) 417–430.
[41] Y. Huo, K. Liu, J. Liu, H. He, Effects of SO2 on standard and fast SCR over CeWO: a quantitative study of the reaction pathway and active sites, Appl. Catal. B Environ. 301 (2022).
[42] W. Tan, J. Wang, L. Li, A. Liu, G. Song, K. Guo, Y. Luo, F. Liu, F. Gao, L. Dong, Gas phase sulfation of ceria-zirconia solid solutions for generating highly efficient and SO2 resistant NH3-SCR catalysts for NO removal, J. Hazard. Mater. 388 (2020), 121729.
[43] Y. Yu, W. Tan, D. An, X. Wang, A. Liu, W. Zou, C. Tang, C. Ge, Q. Tong, J. Sun, L. Dong, Insight into the SO2 resistance mechanism on γ-Fe2O3 catalyst in NH3-SCR reaction: a collaborated experimental and DFT study, Appl. Catal. B Environ. 281 (2021).
[44] J. Liu, R.-t Guo, M.-y Li, P. Sun, S.-m Liu, W.-g Pan, S.-w Liu, X. Sun, Enhancement of the SO2 resistance of Mn/TiO2 SCR catalyst by Eu modification: a mechanism study, Fuel 223 (2018) 385–393.
[45] X. Cheng, X. Wang, C. Ma, J. Wang, W. Qiao, L. Ling, Facile synthesis of Schistose-like Co-Mn oxides for low-temperature catalytic oxidation of NO with enhanced SO2/H2O tolerance, J. Environ. Chem. Eng. 10 (2022).
[46] B. Hammer, J.K. Nørskov, Theoretical surface science and catalysis—calculations and concepts. Advances in Catalysis, Elsevier, 2000, pp. 71–129.